Enhancing the hydrogen evolution properties of kesterite absorber by Si-doping in the surface of CZTS thin film

Enhancing the hydrogen evolution properties of kesterite absorber by Si-doping in the surface of CZTS thin film

Manoj Vishwakarma[1], Mukesh Kumar[2], Mylene Hendrickx[3], Joke Hadermann[3], Aadesh P. Singh[4], Yogita Batra[5], and B. R. Mehta[1*]

[1]Thin Film Laboratory, Department of Physics, IIT Delhi, New Delhi-110016, India
[2]School of Physics and Material Science, Thapar Institute of Engineering &Technology, Patiala-147004, India
[3] EMAT, University of Antwerp, Groenenborgerlaan 171, B-2020 Belgium
[4]Dept. Electronics & Nanoengineering, Aalto University, 02150 Espoo, Finland
[5]J. C. Bose University of Science and Technology, YMCA, Faridabad-121006, India

Abstract

In this work, the effects of Si-doping in Cu_2ZnSnS_4 were examined computationally and experimentally. The DFT calculations showed that an increasing concentration of Si (from x = 0 to x =1) yields a band gap rise due to shifting of the conduction band minimum towards higher energy states in the $Cu_2Zn(Sn_{1-x}Si_x)S_4$. CZTSiS thin film prepared by co-sputtering process shows $Cu_2Zn(Sn_{1-x}Si_x)S_4$ (Si-rich) and Cu_2ZnSnS_4 (S-rich) kesterite phases on the surface and in the bulk of the sample, respectively. A significant change in surface electronic properties has been observed in CZTSiS thin film with an insignificant increase in the band gap. Si-doping in CZTS inverts the band bending at grain-boundaries from downward to upward and the Fermi level of CZTSiS shifts upward. Further, the coating of the CdS and ZnO layer improve the photocurrent to ~5.57 $mA.cm^{-2}$ at -0.41 V_{RHE} in the CZTSiS/CdS/ZnO sample, which is 2.39 times higher than that of pure CZTS. The flat band potential increases from CZTS ~0.43 V_{RHE} to CZTSiS/CdS/ZnO ~1.31 V_{RHE} indicating the faster carrier separation process at the electrode-electrolyte interface in the latter sample. CdS/ZnO layers over CZTSiS significantly reduce the charge transfer resistance at the semiconductor-electrolyte interface in comparison to that of pristine CZTSiS.

Keywords: CZTS, Si-doping, Heterostructure, Photocathode, Photocurrent, Water splitting.

1. Introduction

Sulphur based kesterite Cu_2ZnSnS_4 (CZTS) materials have been examined extensively for solar to energy conversion applications by photovoltaic and photoelectrochemical (PEC) water splitting process.[1-2] CZTS is considered a potential candidate for PEC water splitting application because of its earth abundant, low cost and non-toxic constituents.[3] Oxide semiconductors such as TiO_2 [4] and ZnO [5] have been proven to be stable in electrolyte but show poor absorption due to their large band gap. Semiconductors with a narrow band gap such as Cu_2O [6], WO_3 [7], $BiVO_4$ [8], and α-Fe_2O_3 [9] were also studied, and in this case, chemical instability, low electron conductivity and high photogenerated carrier recombination limit the PEC performance. [10] Among numerous photoelectrodes, the heterostructure photoelectrode emerged as a promising approach to harvest a significant portion of the solar spectrum in addition to generating sufficient photovoltage. [11]

CZTS is a *p*-type semiconductor with suitable opto-electronic properties (absorption coefficient ~ $\alpha \geq 10^4\ cm^{-1}$, band gap ~1.4-1.5 eV) and can be used as a photocathode in PEC water splitting for hydrogen evolution because it can straddle the water oxidation/reduction potential ~1.23 eV.[12] The PEC performance of CZTS depends on the buffer layer (CdS), because CdS over CZTS forms a p-n junction which will facilitate the faster separation of photo-induced e^-/h^+ pairs by the built-in electric field of the junction.[13]

Sn is volatile during the high temperature sulphurization process of CZTS (≥400ºC), resulting in the parallel growth of secondary phases such as SnS and SnS_2. [14] The presence of SnS on the CZTS surface will form an unfavorable band alignment with CdS unlike CZTS, whereas the presence of SnS_2 will form a secondary diode as CZTS-SnS_2. [15-16]

The optimum band gap for solar water splitting is considered to be ~1.9 eV as determined by the energy needed to reduce water (~1.23 eV), plus the thermodynamics loss (~0.4 eV) and over potential required for fast reaction kinetics (~0.3-0.4 eV).[17-18] The kesterite structure provides an opportunity to tune the band gap by substituting or replacing the constituent element in the structure.[18] In a recent study, the Cu_2ZnSiS_4 structure was formed by replacing Sn by Si in CZTS, resulting in a higher band gap ~2.71 eV [19], however, higher than the optimum band gap required for PEC water splitting reaction ~1.9 eV.

Band bending occurs in the CZTS grain boundaries with respect to the grains. It is considered to be of a benign character due to presence of a nanoscale electric field at the grain boundary regions facilitating charge carrier separation, where upward band bending was observed to be better than downward band bending in improving the photovoltaic efficiency of kesterite solar cells. [19-20]

Ge and Si alloying in the kesterite structure is a promising approach to increase the band gap and to suppress Sn associated secondary phases. [21-25] Among all these studies, very few are based on Si substitution compared to the Ge counterpart. In order to understand the role of Si substitution in CZTS for PEC water splitting applications, we first studied the electronic band structure of $Cu_2Zn(Sn_{1-x}Si_x)S_4$ (where x = 0, 0.50, and 1) by first-principle calculations to tune the band gap. We then prepared thin film samples of Si substituted CZTS using rf-magnetron sputtering technique, and analyzed their structure, stoichiometry, surface morphology, surface phases and optoelectronic properties. PEC water splitting measurements were performed to investigate the influence of Si substitution on the photocurrent in the CZTS.

2. Experimental Section

2.1 Computational details

The calculations based on first principle methods were performed using density functional theory (DFT) as implemented in the *plane wave based VASP package* with *PAW* potentials.[26-28] The lattice constants and atomic positions were fully relaxed by *Perdew-Burke-Ernzerhof (PBE)* potential.[29] However, the band gap calculations were performed using the *Heyd-Scuseria-Ernzerhof (HSE06) screened hybrid functional with 25% Fock exchange* and a standard range separation parameter $\omega = 0.2$ to decompose the *Coulomb kernel*.[30] An energy cutoff of *400 eV* and a *Γ-centred homogenous k-point mesh (4×4×4)* were employed in all the cases. We model the kesterite crystalline structure of CZTS with *space group* S_4^2 *(*$I\bar{4}$ *: space group no. 82)* for calculations. To model the alloy structures, Sn was substituted (*Wyckoff positions 2b*) with Si and the structure was relaxed as per standard computational procedure. [31-32] All the calculations were performed for 16 atom cells.

2.2 Experimental details

Thin film synthesis: Kesterite thin film samples were prepared using a magnetron sputtering technique followed by a sulphurization process. Metal targets of Cu, Zn, and Sn were used as a precursor to depositing a *CZT* layer of thickness ~540 nm by the co-sputtering process. The Si substitution was performed by depositing a thin film of Si over the *CZT* layer using sputtering method at *RF power ~70W* for 5 *minutes* while the other sputtering conditions were kept identical to that of the *CZT* layer. This is the optimal time to maintain stoichiometric composition ratios for the kesterite phase. Both pure *CZT* and Si-substituted *CZT* were sulphurized at *~520℃* for *5 minutes* using a closed graphite box containing sulphur powder *(~120 mg)* at *400 Torr Ar* gas pressure. Two samples of pristine CZTS and CZTSiS were prepared using this process. Further, a thin CdS buffer layer was prepared on Mo/CZTS and Mo/CZTSiS thin film samples by using the chemical bath deposition method.[33] The deposition of CdS film was carried out for about *24 minutes* to achieve a thickness of *60-70 nm*.[34] Further, a ZnO thin film (*thickness ~ 50 nm*) was deposited on the Mo/CZTS(CZTSiS)/CdS samples by magnetron sputtering to enhance the stability of the photocathode material in the PEC water splitting applications.[35]

Characterization: The structural analysis was carried out using X-ray diffraction (*Cu K_α, Philips X'pert PRO-PW*) and micro-Raman spectroscopy (*Renishaw invia confocal Raman microscope, laser~532 nm, and 633 nm*). Scanning electron microscopy (SEM) and energy dispersive X-ray measurements on SEM (SEM-EDX) were performed to study the surface structure and stoichiometry of the kesterite samples. The surface analysis was carried out using X-ray photoelectron spectroscopy (XPS; *PerkinElmer PHI 5000 C ESCA system source, monochromatic Al Kα*) to study the chemical states and valence band position in the samples. XPS spectra binding energies were corrected using the C1s standard peak at 284.6 eV.[36] The deconvolution and peak fitting were carried out using the software '*XPSPEAK41*'. The FWHM is kept constant during the peak fitting for each of the doublets of a core spectrum.[36] Low magnification transmission electron microscopy (TEM) images and scanning transmission electron microscopy based EDX (STEM-EDX) were performed using a *Thermo Fisher Osiris* microscope operated at 200kV equipped with a *Super-X detector*. The specimen for the TEM study was prepared using the focused ion beam (FIB) technique, on a gold support. Kelvin probe force microscopy (KPFM) measurements (*Bruker's Dimension ICON Atomic Force Microscopy with Pt/Ir coated cantilever tip*) were carried out to study the effect of Si-doping on the work function of the samples. The

KPFM tip was calibrated by using the work function and measured surface potential (S.P.) of the *HOPG* sample. The relation between the work function of the tip and the *HOPG* is given as, $F_{HOPG} = F_{tip} - e.V_{CPD}$, where, Φ_{HOPG} ~4.8 eV and S.P. of the *HOPG* is observed to be ~25 mV.[36] Hence the work function of the *KPFM tip* is ~ 4.83 eV. The KPFM data is analyzed using *WSxM 4.0 β 8.4* software. The photoelectrochemical water splitting measurements were performed in sodium sulphate Na_2SO_4 (0.5M) electrolyte (pH=6.5) by using a three-electrode PEC cell. The PEC cell consists of Teflon with a quartz window having a working electrode, a Pt counter electrode, and an Ag/AgCl reference electrode. The working electrode is the kesterite thin film with active area ~1 cm^2 which is illuminated by a xenon lamp with intensity 100 mW/cm^2. I-V measurements were performed versus Ag/AgCl by using a potentiostat (*Autolab, Netherlands*), under dark and illumination conditions in the potential range of -1.0 to +1.0 V with a scan rate of 20 mV/s. Mott-Schottky (Capacitance vs potential) measurements were performed in the PEC cell at frequency ~10kHz under dark condition in the potential range of -1.0 to +1.0 V, whereas the EIS measurements are performed under light conditions. The potential conversion from Ag/AgCl to reduced hydrogen electrode (*RHE)* were carried out using the Nernst equation,

$$E_{RHE} = E_{Ag/AgCl} + 0.059pH + E^0_{Ag/AgCl} \quad (1)$$

where $E^0_{Ag/AgCl}$ is the potential of the reference electrode ~0.1976 V at 25ºC and pH indicates the pH value of the electrolyte.

3. Results and discussion

Primarily electronic band structure properties were explored by first-principle calculations. Table-I shows the calculated lattice constants (*a* and *c*), and band gap energies (E_g) of Cu_2ZnSnS_4, $Cu_2ZnSn_{0.5}Si_{0.5}S_4$ and Cu_2ZnSiS_4. The calculated lattice parameters agree well with previously reported data. [37] Due to the small atomic covalent radius of Si (1.10 Å) compared to Sn (1.45 Å) the lattice constants of Cu_2ZnSiS_4 are smaller than those of Cu_2ZnSnS_4.

Table I. Lattice parameters (a, c) and band gap energies (E_g) of Cu_2ZnSnS_4, $Cu_2ZnSn_{0.5}Si_{0.5}S_4$ and Cu_2ZnSiS_4. Values between brackets are literature values [a][24], [b][25].

Compound	a [Å]	c [Å]	E_g [eV]
Cu_2ZnSnS_4	5.441 (5.445)[a]	10.864 (10.858)[a]	1.45 (1.26)[a], (1.48)[b]
$Cu_2ZnSn_{0.5}Si_{0.5}S_4$	5.371 (5.372)[a]	10.637 (10.635)[a]	1.85, (1.87)[a]
Cu_2ZnSiS_4	5.304 (5.307)[a]	10.364 (10.362)[a]	3.05 (3.03)[a], (3.02)[b]

Our calculations yield a band gap of 1.45, 1.85 and 3.05 eV for Cu_2ZnSnS_4, $Cu_2ZnSn_{0.5}Si_{0.5}S_4$ and Cu_2ZnSiS_4, respectively. The calculated band gap values with HSE06 functional agree well with available literature. [24, 37] The increase in the band gap can be inferred from the density of states plots. Figure 1 shows the calculated total density of states (DOS) for all three structures. One can see that the conduction band minimum (CBM) of the kesterite material is shifted towards the higher energy on the incorporation of Si in the structure [Figure. 1(b)]. The CBM is dominated by hybridization of the S-*p* and Sn-*s* orbitals, similarly the valence band maximum (VBM) is dominated by the Cu-3*d* and S-*p* hybridization. [38] Therefore, the increase in the band gap of the material can be attributed to the modification in the density of states near the CBM where changes occur in the chemical environment (from Sn to Si). This is because, in CZTS, the lowest conduction band is separated from the higher energy bands and can therefore be more localized in energy. [38] Due to this localized conduction band in CZTS, it was expected that the energy position of the Sn-s and S-p DOS peak can be varied in energy by alloying on the Sn-site with other group-IV elements, like for instance Si or Ge. Thereby, the band-gap energy can be tailored by cation alloying for an optimized energy gap. Overall, hybrid functional (HSE06) based DFT calculations predict the increase in the band gap of kesterite CZTS with increasing Si concentration on the Sn site.

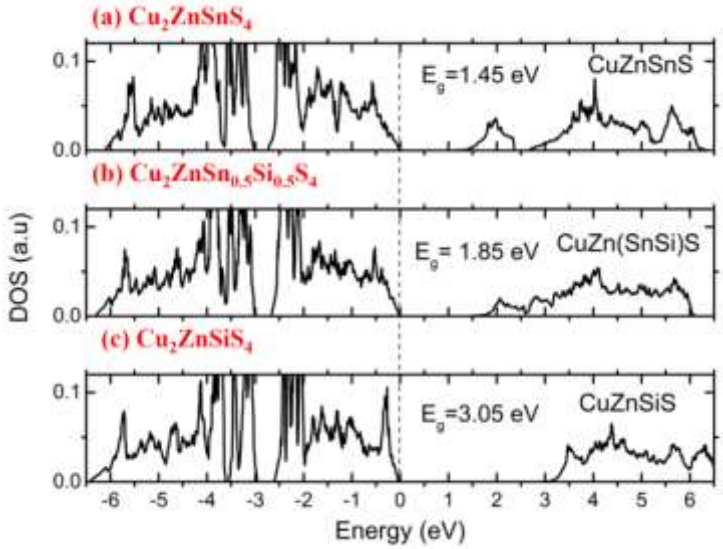

Figure. 1 Calculated density of states for (a) Cu_2ZnSnS_4, (b) $Cu_2ZnSn_{0.5}Si_{0.5}S_4$ and (c) Cu_2ZnSiS_4.

Table II. Composition analysis of the thin film samples by EDX measurements.

Samples	**Atomic %**				***Cu/(Sn+Si)***	***Si/(Sn+Si)***	***Zn/(Sn+Si)***	***Cu/(Zn+Sn+Si)***
	Cu	**Zn**	**Sn**	**Si**				
CZTS	49.4	30.2	20.5	0	2.41	0	1.47	0.97
CZTSiS	44.1	26	19.5	11.1	1.44	0.36	0.85	0.78

Compositional analysis of the kesterite samples was carried out by using SEM-EDX (Table II). The Si substitution in the CZTSiS sample causes a decrease in the relative concentration of Cu, Zn, and Sn with respect to that of CZTS sample. The composition ratios in the CZTS are Cu/[Zn+Sn]~0.97, Zn/Sn~1.47, whereas in CZTSiS are Cu/[Zn+Sn+Si]~0.78, Zn/[Sn+Si]~0.85 (Table II).[34] Since the Si is added in the CZTS without changing the concentrations of other cations [Cu, Zn, Sn], stoichiometry ratio was decreased. Therefore, the alloying and distribution of Si in the kesterite thin film will be more important rather than its optimum concentration with respect to stoichiometry ratio. The SEM Micrographs (Figure. 2) revealed a variation in surface structure in both the CZTS and CZTSiS samples. The surface of the CZTSiS thin film [Figure. 2 (c-d)] is dominated by grains of elongated shape (sizes~500 nm-3 μm) in comparison to that of the

CZTS thin film. These elongated particles emerged due to Si substitution in the kesterite sample. Such kind of grains were also observed by Hamdi *et al*. for $Cu_2Zn(Sn,Si)S_4$.[25] The effect of Si-doping on the bulk structural properties was studied by XRD and Raman analysis. The XRD spectra [Figure. 3 (a)] recorded on both samples agree with the kesterite phase (JCPDS no. 26-0575). Since the Si-content [*Si/(Sn+Si)~0.36*] in the *CZTSiS* sample is lower than *0.5, $Cu_2ZnSn_xSi_{1-x}S_4$* phase will crystallize in CZTS type structure and will represent identical XRD reflections as that of CZTS sample [Figure 3 (a)].[25] DFT calculations show apparent lattice constant reduction of CZTS (*a=5.441Å, c=10.864 Å*) to CZTSiS (*a=5.371Å, c=10.637 Å*) but experimentally cell parameters will not undergo significant change in the $Cu_2ZnSn_xSi_{1-x}S_4$ if Si-concentration is *Si/(Sn+Si) <0.8* in the sample, as suggested by Hamdi *et al*.[25] There were no peaks of any secondary phases. The bulk structure cannot be distinguished by XRD analysis because both CZTS and Cu_2ZnSiS_4 have a similar tetragonal structure.[19] Identification of secondary phases by Raman spectra under different excitation wavelengths is considered to be a powerful tool due to the variations in the vibrational displacements which are imposed by the symmetry of the lattice.[19, 39] In both the samples, the Raman spectra (~532 nm excitation laser) [Figure. 3 (b)] show peaks at 286 cm^{-1} and 337 cm^{-1}, while spectra with ~633 nm excitation wavelength [Figure. 3 (c)] show peaks at 264, 286, 304, 337, and 367 cm^{-1} corresponding to the kesterite phase.[19, 39-40] The Raman shifts observed at 264, 286, 304, 337 cm^{-1} belong to A symmetry mode whereas peak at 367 cm^{-1} corresponds to B symmetry mode of kesterite phase.[19, 39-40] Since *Cu_2ZnSiS_4* and *Cu_2ZnSnS_4* phases show identical Raman shifts at 264, 286, 304, and 337 cm^{-1}, *$Cu_2ZnSn_xSi_{1-x}S_4$* phase could not be distinguished from CZTS.[41] However, no sulphide phase was detected other than primary kesterite phase by Raman analysis, confirming the single kesterite phase in the samples.

Further, the transmittance spectra were recorded by using UV-visible spectroscopy in order to study the effect of Si substitution on the optical absorption properties in the samples. The absorption coefficient [α (cm^{-1})] is calculated as,

$$\alpha = \frac{1}{d}\ln\left(1/T\right), \tag{2}$$

where d is the thickness of the film (~1.4 μm) and T is the transmission.[42] The absorption coefficient of semiconducting material is related to photon energy (hν) by the following formula,

$$(\alpha h\nu) = b\left(h\nu - E_g\right)^n, \tag{3}$$

where β is the band tailing parameter, E_g is the band gap energy and n is a power factor depending on the type of optical transitions (1/2 for direct band gap, 0 and 2 for indirect band gap semiconductor materials).[42]

In the present case, we use n=1/2 as CZTS is a direct band gap semiconductor.[42] The band gap calculated by Tauc plots is 1.44 and 1.47 eV, for samples CZTS and CZTSiS, respectively [Figure. 3 (d)]. The transmission edge shifts towards lower wavelength on Si substitution in the CZTS sample which indicates an increase in the band gap of the sample CZTSiS [Inset of Figure. 3 (d)]. The increase in band gap is relevant with the theoretical results as shown in Figure. 1(b). In order to investigate the distribution of Si across the kesterite thin film, cross-sectional TEM measurements were performed. The quantification of the compositions across the cross-sectional lamella of the CZTSiS sample was carried out using STEM-EDX, and the corresponding mixed and individual elemental maps are shown in Figure 4.

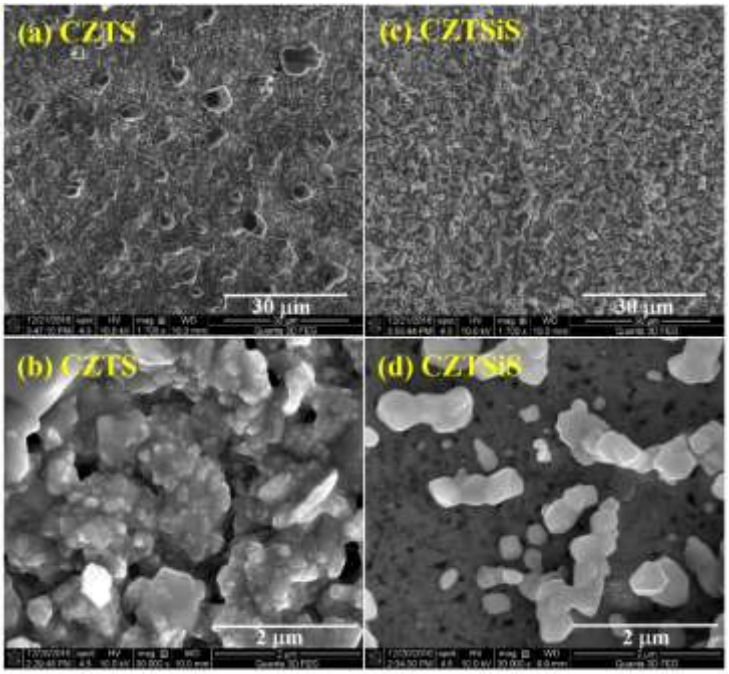

Figure. 2 SEM micrographs for samples (a-b) CZTS and (c-d) CZTSiS.

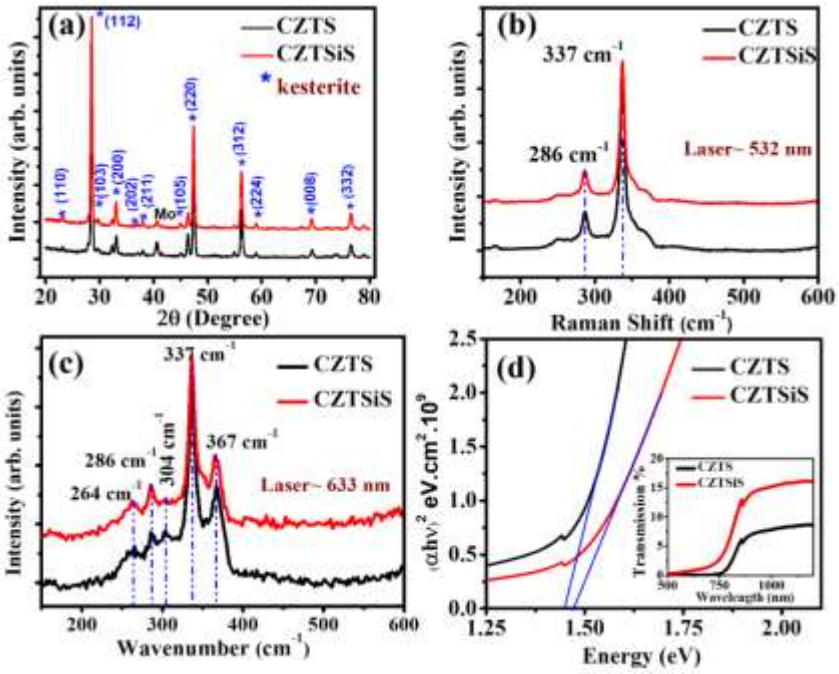

Figure. 3 (a) XRD spectra, and Raman spectra at (b) 532 nm, (c) 633 nm laser excitation sources, (d) Tauc plots of kesterite thin film samples. Inset in figure (d) shows the transmission spectra of the samples, CZTS and CZTSiS.

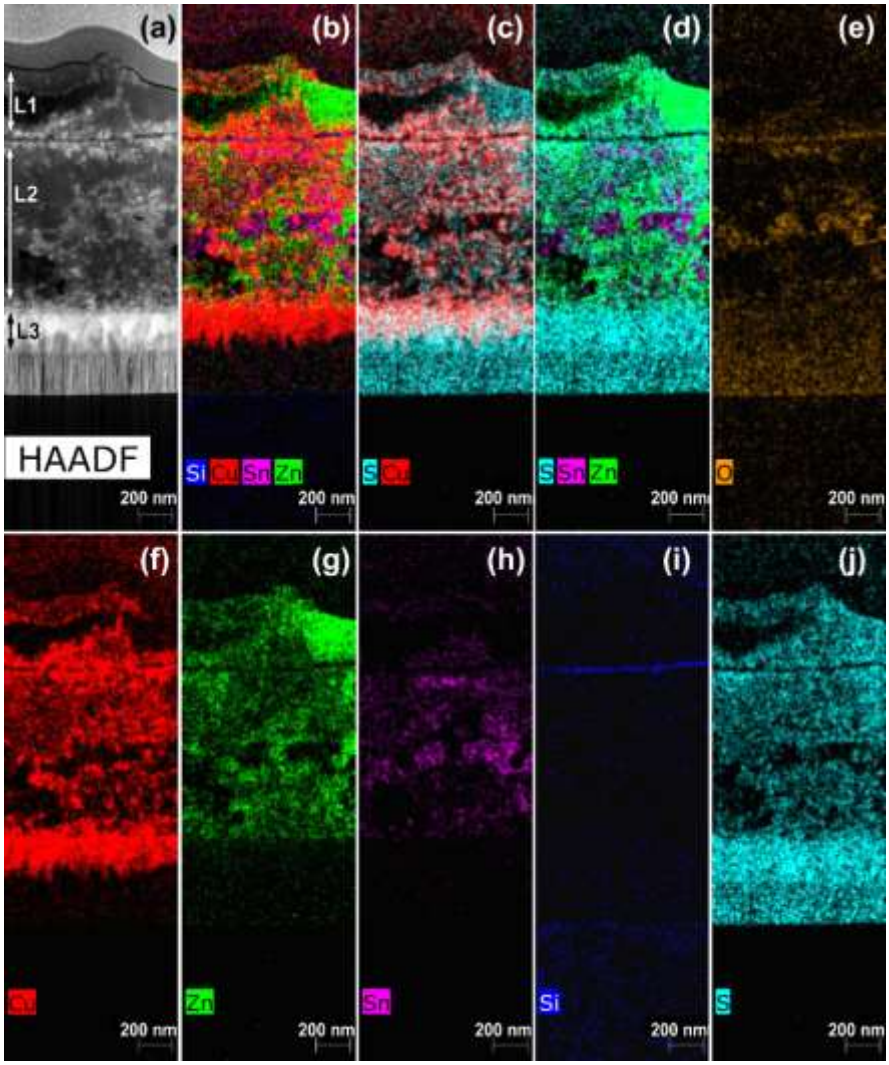

Figure. 4 Left to Right: (a) HAADF image of the cross-sectional lamella of the CZTSiS sample, (b) mixed cation map {Si, Cu, Sn, Zn}, (c-d) cation-anion maps ({S, Cu}, {S, Sn, Zn}), and (e-j) individual elemental maps of the elements O/Cu/Zn/Sn/Si/S. All maps are given in atomic percentage.

The STEM-EDX study showed that the kesterite absorber layer consists of two layers, indicated as L1 (~380 ± 80 nm) and L2 (~900 ± 50 nm). For both layers, the main phase corresponds to the kesterite phase CZTS, but without Si. The Si is segregated to the interface between these two layers and forms a SiO_2 layer with a thickness of ~30 ± 10 nm. Further, the cation-anion maps {S, Cu} and {S, Sn, Zn} reveal the presence of nanoscale secondary phases (Figure. 4). The {Cu, S} map indicates the presence of bright red contrast in the shape of nanoparticles which can be seen in layers L1 and L2 and are attributed to Cu_xS ($x \approx 2$). The bright green contrast in the {S, Sn, Zn}

map near the top of layer L1 indicates the presence of ZnS. Comparing the {S, Sn, Zn} and O map shows the formation of SnO_x ($x \approx 2$) particles, which were only present in L2. Between these two layers and the Mo layer of the thin film, there is an additional third layer (L3), which only consists of Cu_2S particles and partially overlap with the Mo layer. The growth of nanoscale secondary phases can be attributed to the small area of the kesterite phase in the phase diagram.[43] Whereas SEM-EDX analysis provides the average composition ratio over all the phases presenting in the CZTSiS thin film, STEM-EDX mapping identified the location of different phases across the cross-section. Although XRD and Raman analysis indicate the presence of pure kesterite phase in the sample CZTSiS, there are nanoscale secondary phases across the cross-section of the thin film. Moreover, the Si substitution is not alloying in the bulk of the CZTSiS thin film, as observed in the TEM investigations. However, SEM analysis has shown that Si-doping significantly modifies the surface morphology of the sample CZTSiS which was further investigated by XPS measurements.

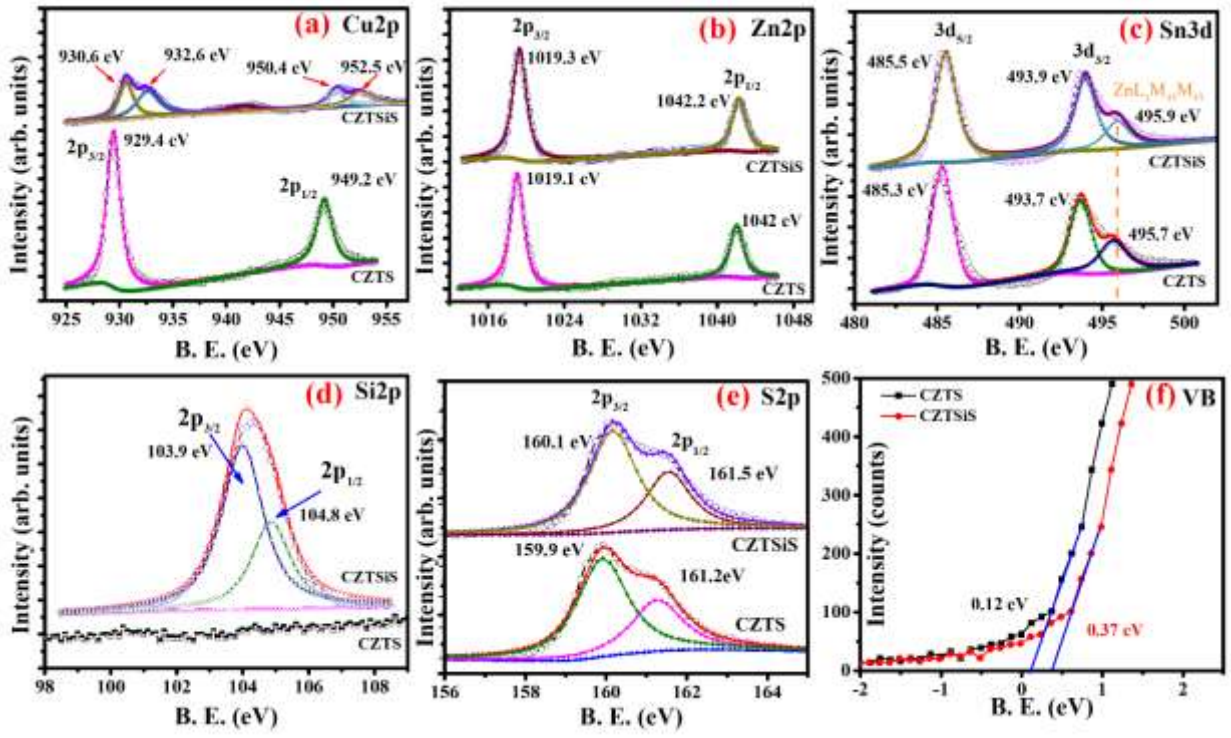

Figure. 5 XPS core-level spectra of (a) Cu2p, (b) Zn2p, (c) Sn3d, (d) Si2p, (e) S2p, and (f) Valence band of CZTS and CZTSiS.

XPS measurements were performed to study the chemical and compositional analysis on the surface of the kesterite thin films. The core-level spectra of the Cu, Zn, Sn, Si, and S are shown in Figure 5. The spin-orbit energy splitting (ΔE) is the difference of binding energies of the doublet for the core-spectrum with spin s= ±1/2 in an element.[44] The $Cu2p_{3/2}$ state in the CZTS sample was observed at binding energy ~929.4 eV with ΔE ~19.8 eV [Figure. 5 (a), lower figure]. The $Cu2p_{3/2}$ core level in the sample CZTSiS shows two states corresponding to binding energies, 930.6 and 932.6 eV with ΔE ~19.8 and 19.9 eV, respectively [Figure. 5(a), upper figure]. The Cu2p peaks observed at binding energies, 929.4, 930.6 and, 932.6 eV can be assigned for Cu(I) state in both samples as the peak owing to Cu(II) state at binding energy ~934 eV is completely absent in the Cu2p core-level spectrum.[45-46] In general, Cu_2S and CZTS both are found in Cu(I) state but Cu_2S was detected neither in the Raman spectra nor in the XRD, thus Cu(I) state solely presents in the lattice of kesterite phase on the surface of thin film samples [Figure. 5 (a)]. Core-level spectra of Zn2p show $2p_{3/2}$ states at binding energies ~1019.1 eV and 1019.3 eV for samples CZTS and CZTSiS, respectively with ΔE ~22.9 eV which can be attributed to Zn(II) state in the samples [Figure. 5 (b)].[45-46] As Zn(II) state is found in the CZTS as well as in the ZnS, thus these two phases cannot be distinguished by XPS interpretation, and according to the TEM analysis, ZnS is indeed present along with the kesterite phase near the surface. Sn3d states were observed at binding energies $Sn3d_{5/2}$ ~485.3 and 485.5 eV, with ΔE ~8.4 eV, for samples CZTS and CZTSiS, respectively, which can be assigned to Sn(IV) state [Figure. 5 (c)].[45-46] The Si2p peak was observed at $2p_{3/2}$ ~103.9 eV with ΔE ~0.9 eV in the sample CZTSiS [Figure. 5 (d)]. The Si2p doublet at binding energies 103.9 and 104.8 eV can be assigned to the Si(IV) state in the Si-doped kesterite sample, whereas it is completely absent in the CZTS sample .[19] Moreover, the core-spectrum for S2p state was found at binding energy $2p_{3/2}$ ~159.9 eV with ΔE ~1.3 eV for the sample CZTS, while it was observed at 160.1 eV with ΔE ~1.4 eV for the sample CZTSiS [Figure. 5 (e)]. The S2p doublets (159.9/161.2 eV) and (160.1/161.5 eV) can be assigned to the $S(II^-)$ state in the samples CZTS and CZTSiS, respectively.[45-46] The S2p state was observed to shift towards higher binding energy in case of Si-doped CZTS sample, which may be due to the Si-S bonding in the CZTSiS structure.[45-46] Since the sample CZTS is without Si concentration, the peak corresponding to Si2p was not observed in the spectrum. The XPS analysis confirms the formation of Cu^+, Zn^{2+}, Sn^{4+}, Si^{4+} and S^{2-} species on the surface of the CZTSiS sample. As there is a shift in the Cu2p peaks towards higher binding energy on Si incorporation, the shift can be attributed to

the formation of $Cu_2Zn(Sn_{1-x}Si_x)S_4$ phase in the CZTSiS sample.[19] From XPS measurement, it can be concluded that the $Cu_2ZnSn_{1-x}Si_xS_4$ phase is formed on the surface of Si-doped thin film sample. Further, a valence band study was carried out to study the shift in Fermi level due to Si incorporation in the CZTS sample [Figure. 5 (f)]. The Fermi level position of the samples CZTS and CZTSiS were determined to be ~ 0.12 and 0.37, respectively. The Fermi levels were observed to significantly shift towards conduction band minima on Si-doping in the kesterite thin films. Hence, the shift in Fermi levels is in good agreement with the theoretical calculation of density of states for $Cu_2Zn(Sn_xSi_{1-x})S_4$ [Figure. 1(b)]. XPS core-level and the valence band analysis validate the kesterite phase in the CZTSiS sample. Therefore, the two kesterite phases, Cu_2ZnSnS_4 and $Cu_2Zn(Sn_xSi_{1-x})S_4$ are present in the CZTSiS thin film sample. Hence, the increase in band gap is very small because Si incorporation in the CZTS thin films alloy with the top surface only, as revealed by XPS analysis, whereas the Tauc plot calculate the bandgap for the whole thickness of the sample.

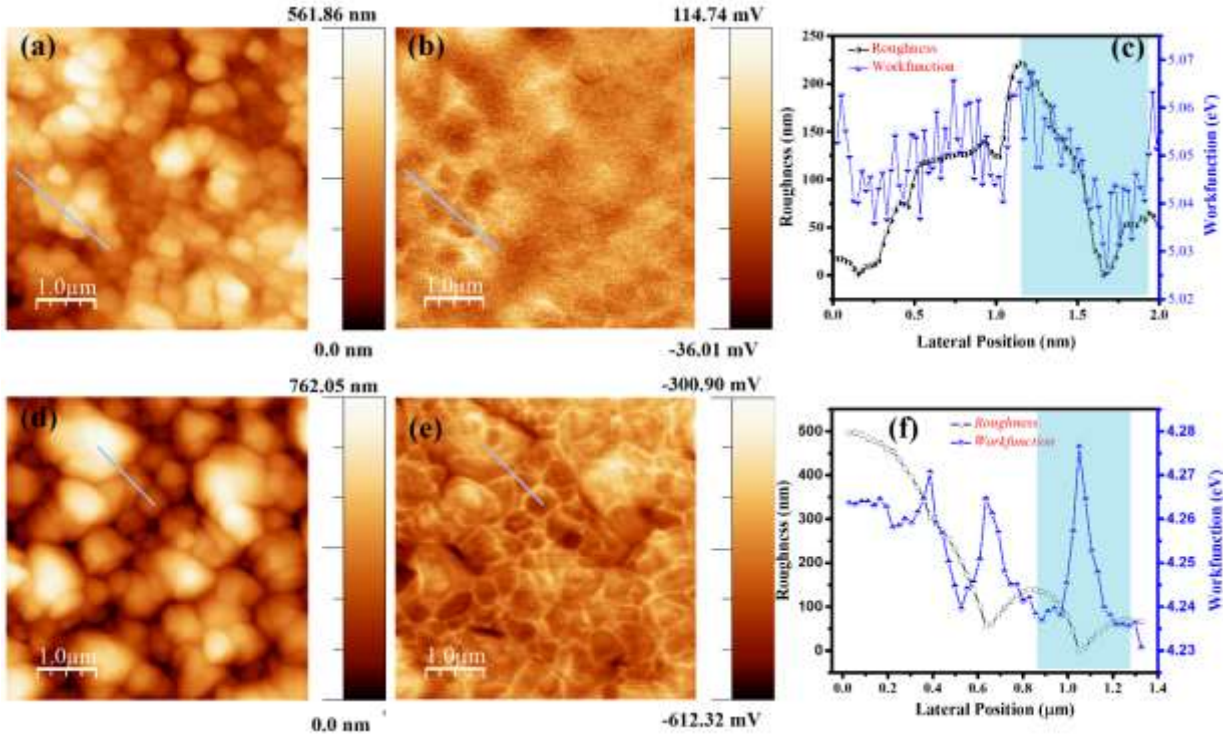

Figure. 6 CZTS; (a) Surface morphology, (b) KPFM map, (c) Line profile across the morphology and potential maps. CZTSiS (d) Surface morphology, (e) KPFM map, (f) Line profile across the morphology and potential maps.

Further, the effect of Si substitution on the surface electrical properties was investigated by KPFM measurements (Figure. 6). In Figure 6, the morphology and surface potential images are shown for CZTS and CZTSiS, samples. The work function of a sample is calculated by using the relation,

$$F_{Sample} = F_{tip} \pm e.(S.P.) \quad (3)$$

where Φ_{Sample} and Φ_{tip} are the work functions of the sample and KPFM tip, respectively.[36] The positive and negative signs indicate the bias is applied to the sample and tip, respectively. The bias voltage was applied on the tip in case of CZTS whereas it was applied to the sample for CZTSiS. However, altering the bias voltage does not affect the final values of the work function for any kind of samples. Figure 6 (c, f) shows the line profiles for CZTS and CZTSiS, which indicate the band bending on grain boundaries to grain. The work function varies from grain to grain boundaries in the typical range of ~5.03-5.07 eV and 4.23-4.27 eV for samples CZTS and CZTSiS, respectively [Figure. 6 (c, f)]. To understand the behavior of band bending, we have selected a region from one grain to another grain in the Figure. 6 (c, f)], as highlighted by light blue color. By using the values of the bandgap, work function, and Fermi energy, the energy band diagram of the material can be proposed. A schematic of the energy band diagram and band bending of the CZTS, CZTSiS samples are given in figure 7.

CZTSiS shows a higher work function at the grain boundaries than the grains, which indicates upward band bending, while CZTS shows a lower work-function at the grain boundaries than the grains, which indicates downward band bending (Figure. 7). The downward band bending at grain boundaries attracts electrons and repels holes while it will show reverse behavior for the charge carriers in the CZTSiS grain boundaries as can be seen by the schematic of band bending in Figure 7. Two consecutive grain boundaries are at a distance ~ 790 nm in CZTS, ~450 nm in CZTSiS, approximately as highlighted by a rectangle in figure 6 (c, f). Although the width of the grain boundaries reduces from CZTS to CZTSiS, the potential difference between grain and grain boundaries has the same value (~40 mV). Therefore, the Si-substitution not only inverts the band bending but also makes the grain boundaries channel more confined which effectively traps the photogenerated holes and reduces the recombination process in the kesterite sample. Moreover, the upward band bending at the grain boundaries with respect to the grain is considered to have better photovoltaic efficiency than the downward bending at the grain boundaries which can also play a crucial role in the improvement of the hydrogen evolution of the photocathode.[20]

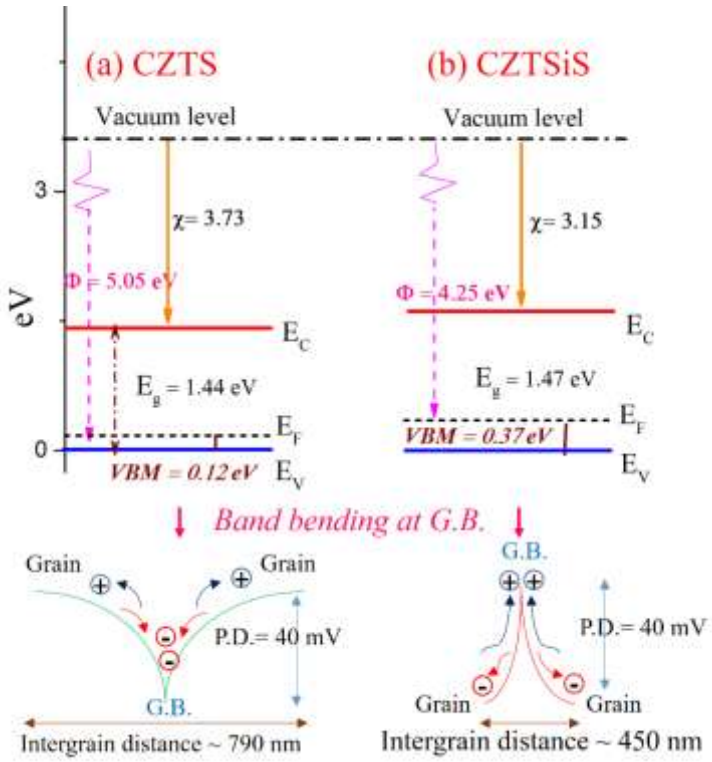

Figure. 7 Energy band diagrams of (a) CZTS, (b) CZTSiS. Below the energy band diagrams showing band bending at grain boundaries (G.B.) with respect to grain.

The work function and Fermi level are crucial parameters for any absorber material used to fabricate heterostructure PEC devices because the band alignment and band bending are explained by these parameters. [19] Further, the prepared heterostructure devices were tested for PEC water splitting applications. Figure 8(a) shows cross-sectional FESEM image of CZTSiS/CdS/ZnO sample confirming the formation of heterostructure photocathode. Figure 8(b) shows the photocurrent density-potential curves of the CZTS, CZTSiS, CZTS/CdS/ZnO, and CZTSiS/CdS/ZnO samples. All the photocathode samples provide a cathodic photocurrent behaviour revealing p-type semiconducting properties of the absorber material. The bare CZTS thin film sample shows the photocurrent density ~1.96 $mAcm^{-2}$ at -0.40 V_{RHE} and it is improved to ~2.53 $mAcm^{-2}$ at -0.40 V_{RHE} in the case of CZTSiS sample. In dual absorber system, lower band gap CZTS allows the absorption of even those photons which are otherwise not absorbed in the higher band gap material, providing additional photovoltage to facilitate PEC water splitting process.[47] However, the minor improvement in the photocurrent density in the CZTSiS is because $Cu_2Zn(Sn_{1-x}Si_x)S_4$ formed only on the surface of the sample. To improve the water-splitting

activity, a thin layer of n-type CdS buffer layer was coated over the kesterite thin film to form a p-n junction.[34]

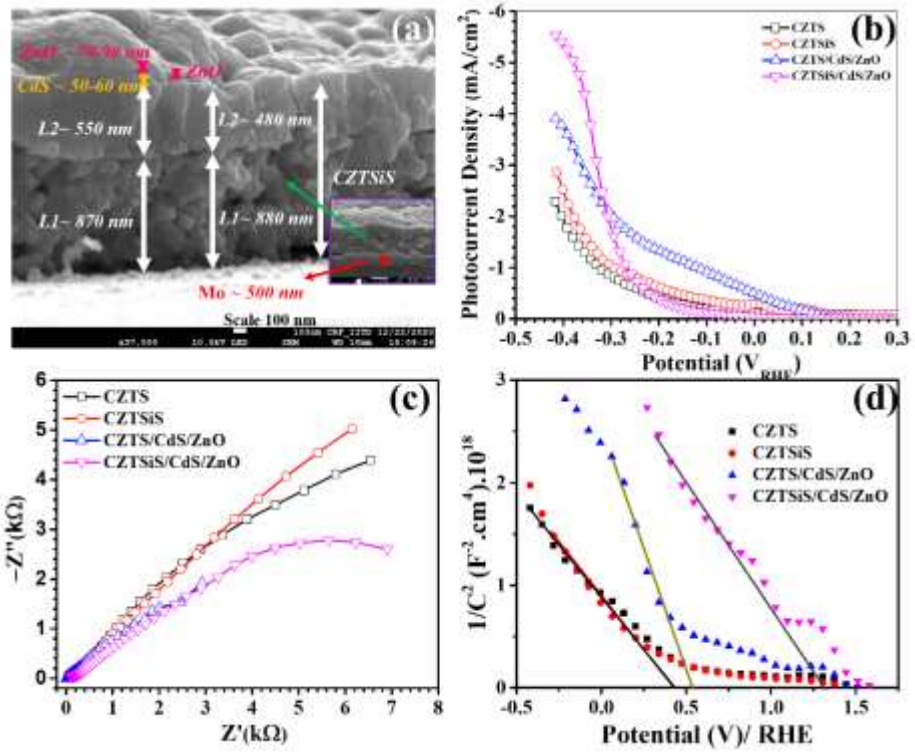

Figure. 8 (a) Cross-sectional image of CZTSiS/CdS/ZnO sample (Figure 1S), (b) Current density-potential curve, (c) Nyquist plots, and (d) Mott-Schottky plots of the CZTS, CZTSiS, CZTS/CdS/ZnO, and CZTSiS/CdS/ZnO photocathode samples in a sodium sulphate aqueous solution (pH= 6.5).

The thickness of the CdS layer can be controlled by optimizing the chemical bath deposition reaction time because it significantly influences the heterostructure device performance.[34] CdS thin film directly exposed to electrolyte faces severe photocorrosion.[48] A thin ZnO layer can provide chemical stability in the heterostructure photoelectrode.[48-49] A thin layer of ZnO (60-70 nm) was prepared by magnetron sputtering over the buffer layer in the kesterite thin film samples. The zinc-oxide layer acts as a protecting layer and blocks the shunt path across the Mo-back contact and electrolyte in kesterite-CdS photocathode samples. Furthermore, ZnO is considered favorable for water reduction process, which allows the flow of electrons from CdS towards semiconductor-electrolyte interface and reverse flow of holes enhancing the hydrogen evolution performance. [49-50] The p-n junction creates built-in potential across the junction due to equilibrium

of the Fermi levels in the depletion width. The depletion width induces sharp potential step across the band bending, facilitating the charge carrier separation and shifting the onset potential towards the anodic side.[50-51] In Figure 8(a), PEC properties of the heterostructure kesterite samples have also been measured under similar experimental conditions. The improvement in the photocurrent density was achieved by deposition of the buffer layer (CdS), followed by the protecting layer (ZnO). The photocurrent density of the CZTS/CdS/ZnO electrode was 3.75 $mA.cm^{-2}$ at -0.40 V_{RHE} which is 1.9 times higher than that of pristine CZTS sample. The photocurrent density of the CZTSiS/CdS/ZnO reached 5.41 $mAcm^{-2}$ at -0.40 V_{RHE}, which is 2.8 and 2.1 times higher than that of pure CZTS and CZTSiS, respectively. Two depletion regions (kesterite layer/CdS and electrode-electrolyte interface) present in the heterostructure samples allow the formation of photogenerated e^{-}-h^{+} pairs within the photoelectrode and near the surface.[52] It can be noticed that Si-doped samples show improved photocurrent density in both kinds of samples, pristine and heterostructure photocathodes. Enhancement in the PEC performance in Si-doped samples can be attributed to the steep band bending at grain boundaries of the absorber in contrast to that of CZTS (Figure. 7). The sharp potential difference at grain boundaries with respect to the grains in the CZTSiS sample induces faster carrier separation near the grain boundaries and effectively reduces the recombination of photogenerated charge carriers. [20] Moreover, the upward band bending at the grain boundaries of the CZTSiS in contrast to CZTS is considered to be of a benign character for improved photovoltaic efficiency. [20]

The interfacial electron transfer kinetics of photogenerated charge carriers was also studied using EIS measurements.[53] Figure 8 (c) shows the Nyquist plots of all the four samples, CZTS, CZTSiS, CZTS/CdS/ZnO, and CZTSiS/CdS/ZnO. Although the arc radius of CZTSiS photocathodes is higher than that of pristine CZTS photocathodes, it decreases for the samples coated with CdS/ZnO layers. Since the smaller radius of the Nyquist plot indicates lower resistance for the electron transfer at the electrode-electrolyte interface, the buffer layer and protecting layer enhance the transport of the photo-generated charge carriers from the electrode to electrolyte.[53] Therefore, from EIS measurement, it is observed that kinetics of charge transfer improved in the CdS/ZnO coated CZTS and CZTSiS samples. Further, the flat band potential of semiconductor is considered to be a crucial physical parameter in order to understand the transition of charge carriers at the photoelectrode-electrolyte interface. Therefore, capacitance-voltage (C-V) measurements were carried out under dark condition at the fixed frequency of ~10 kHz. The potential was scanned

from -1.0V to 1.0V (Ag/AgCl) which is further converted in RHE by using equation (1). Then space-charge capacitance at the semiconductor/electrolyte interface varies with the applied potential according to the Mott- Schottky equation:

$$\frac{1}{C^2} = \left(\frac{2}{q\varepsilon\varepsilon_o\varepsilon_s A^2 N_d}\right)\left(V_{app} - V_{fb} - \frac{kT}{q}\right) \quad (4)$$

where, C, N_d, q, ε_0, ε_s, A, V_{app}, V_{fb}, k,and T are space-charge capacitance (F), donor density (cm^{-3}), electronic charge ($1.6x10^{-19}$C), vacuum permittivity ($8.854x10^{-12}$ Fm^{-1}), relative permittivity of semiconductor, active photoelectrode area (cm^2), applied bias voltage (V), flat band potential (V), Boltzmann constant ($1.38x10^{-23}$ $J.K^{-1}$), and T is the temperature (298 K).[52] Mott-Schottky curves of all the samples are shown in Figure. 8 (d) indicating the negative slopes, which are in good agreement with the p-type nature of the photocathode absorber.[52] In the case of non-linear M-S plot, the linear portion of the curve can be fitted (over potential range $\Delta V > 200$ mV), which is induced from the dominating bulk built in potential or bulk electrode-electrolyte interface potential.[52, 54-55] The linear region extrapolated to $\frac{1}{C^2} = 0$ provides the correct flat band potential value.[52, 54-55] The flat band potentials of the samples, CZTS, CZTSiS, CZTS/CdS/ZnO, and CZTSiS/CdS/ZnO are found as 0.43V, 0.43V, 0.53V, and 1.31 V, respectively [Figure. 8 (d)]. The similar flat band potential values were observed for CZTS, and CZTSiS photocathodes, which can be due to the presence of bulk CZTS phase in both the samples. However, the flat band potential of heterostructure photocathode sample CZTSiS/CdS/ZnO significantly increased in comparison to that of CZTS/CdS/ZnO sample because the surface modification and grain boundaries band bending critically affects the photovoltaic performance in the CZTS (CZTSiS)/CdS based junction devices.[56] The shifting of the flat band potential towards the higher potential side can be attributed to the modification in the electronic structure of the photocathode samples. Since the higher flat band potential facilitates the applied bias induced band bending at the semiconductor-electrolyte interface, the CZTSiS/CdS/ZnO photocathode induces better charge carrier separation at the interface.[57] Therefore, Si- substitution in the kesterite samples results in the improvement of photocurrent density owing to following investigated factors, (i) the higher band gap kesterite phase on the surface, (ii) steep potential difference between grain and grain boundaries, (iii) upward band bending, (iv) application of buffer and protecting layers.

4. Conclusions

The effects of the substitution of Sn by Si atoms on the structural, electronic, optical and electrical properties of CZTS thin films were investigated computationally, and experimentally. A band gap rise in $Cu_2Zn(Sn_{1-x}Si_x)S_4$ was observed with increasing Si-concentration in theoretical calculations. By using a one-step sulphurization process of the precursor thin film (Cu-Zn-Sn)/Si, Si-alloyed kesterite phase $Cu_2Zn(Sn_{1-x}Si_x)S_4$ resulted on the surface of the thin film without changing the bulk CZTS phase. The bulk phase can be identified by XRD, Raman, and TEM analysis but the surface modification was revealed by XPS and KPFM investigations where band alignment parameters and grain boundary electrical properties were significantly changed. Further, CZTSiS photocathode with CdS/ZnO coating significantly enhances the photocurrent and bias assisted band bending at the electrode-electrolyte interface compared to pristine CZTS. The dual absorber system Cu_2ZnSnS_4 - $Cu_2ZnSn_xSi_{1-x}S_4$ in the material CZTSiS provides improved photon absorption, which can significantly improve the performance of water splitting and photovoltaic devices. Moreover, the band gap for pure $Cu_2ZnSn_xSi_{1-x}S_4$ phase is 1.86 eV which is considered to be optimum energy gap for water splitting process.

Acknowledgment

Authors acknowledge support provided by DST in the forms of Nano-Mission and InSOL project. Prof. B.R. Mehta acknowledges the support of the Schlumberger chair professorship. M.V. also acknowledges the support of DST-FIST Raman facility. A.P.S. gratefully acknowledges the financial support provided by the Academy of Finland.

References:

[1] B. Shin, O. Gunawan, Y. Zhu, N. A. Bojarczuk, S. J. Chey, S. Guha, *Prog. Photovolt: Res. Appl.* **2013**, 21, 72.

[2]E. Ha, L. Y. S. Lee, J. Wang, F. Li, K. Y. Wong, S. C. E. Tsang, Adv. Mater. 2014, 26, 3496.

[3]J. Paier, R. Asahi, A. Nagoya, G. *Kresse, Phy. Rev.* B **2009**, 79, 115126.

[4] Z. Zhang, L. Zhang, M.N. Hedhili, H. Zhang, P. Wang, *Nano Lett.* **2013**, 13, 14.

[5] Y. Qiu, K. Yan, H. Deng, S. Yang, *Nano Lett.* **2011**, 12, 407.

[6] A. Paracchino, N. Mathews, T. Hisatomi, M. Stefik, S.D. Tilley, M. Gratzel, Energy Environ. Sci. **2012**, 5, 8673.

[7] Y. Hou, F. Zuo, A. P. Dagg, J. Liu, P. Feng, *Adv. Mater.* **2014**, 26, 5043.

[8] T. W. Kim, K. S. Choi, *Science* **2014**, 343, 990.

[9] P. Zhang, A. K. Shwarsctein, Y. S. Hu, J. Lefton, S. Sharma, A. J. Forman, E. M. Farland, *Energy Environ. Sci.* **2011**, 4, 4862.

[10] A. Paracchino, V. Laporte, K. Sivula, M. Grätzel, E. Thimsen, *Nater. Mater.* **2011**, 10, 456.

[11] J. Wang, N. Yu, Y. Zhang, Y. Zhu, L. Fu, P. Zhang, L. Gao, Y. Wu, *J. Alloys Compd.* **2016**, 688, 923.

[12] M. G. Walter, E. L. Warren, J. R. M. Kone, S. W. Boettcher, Q. Mi, E. A. Santori, N. S. Lewis, *Chem. Rev.* **2010**, 110, 6446.

[13] N. Guijarro, M. S. Prevot, X. A. Jeanbourquin, X. Yu, K. Sivula, *Chem. Mater.* **2015**, 27, 6337.

[14] J. J. Scragg, T. Ericson, T. Kubart, M. Edoff, C. P. Bjorkman, *Chem. Mater.* **2011**, 23, 4625.

[15] K. F. Tai, O. Gunawan, M. Kuwahara, S. Chen, S. G. Mhaisalkar, C. H. A. Huan, D. B. Mitzi, *Adv. Energy Mater.* **2016**, 6, 1501609.

[16] D. Lim, H. Suh, M. Suryawanshi, G. Y. Song, J. Y. Cho, J. H. Kim, J. H. Jang, C. W. Jeon, A. Cho, S. Ahn, J. Heo, *Adv. Energy Mater.* **2018**, 8 (10), 1702605.

[17] J. R. Bolton, S. J. Strickler, J. S. Connolly, *Nature* **1985**, 316, 495.

[18] C. Ros, T. Andreu, S. Giraldo, V. I. Roca, E. Saucedo, J. R. Morante, *ACS Appl. Mater. Interfaces* **2018**, 10, 13425.

[19] M. Vishwakarma, D. Varandani, S.M. Shivaprasad, B.R. Mehta, *Sol. Energy Mater. Sol. Cells* **2018**, 174, 577.

[20] A. H. Xin, S. M. Vorahl, A. D. Collord, I. L. Braly, A. R. Uhl, B. W. Krueger, D. S. Ginger, H. W. Hillhouse, *Phys. Chem. Phys.* **2015**, 17, 23859.

[21] D. B. Khadka, J. H. Kim, *J. Phys. Chem. C* **2015**,119, 1706.

[22] C. J. Hages, S. Levcenco, C. K. Miskin, J. H. Alsmeier, D. A. Ras, R. G. Wilks, M. Bar, T. Unold, R. Agrawal, *Prog. Photovoltaics Res. Appl.* **2015**, 23(3) 376.

[23] Q. Shu, J. H. Yang, S. Chen, B. Huang, H. Xiang, X. G. Gong, S. H. Wei, *Phy. Rev. B* **2013**, 87, 115208.

[24] H. R. Liu, S. Chen, Y. T. Zhai, H. J. Xiang, X. G. Cong, S. H. Wei, *J. Appl. Phy.* **2012**, 112, 093717.

[25] M. Hamdi, A. Lafond, C. G. Deudon, F. Hlel, M. Gargouri, S. Jobic, *J. Solid State Chem.* **2014**, 220, 232.

[26] G. Kresse, J. Furthmüller, *Phys. Rev. B* **1996**, 54, 11169.

[27] G. Kresse, J. Furthmüller, *Comput. Mater. Sci.* **1996**, 6, 15.

[28] G. Kresse, D. Joubert, *Phys. Rev. B* **1999**, 59, 1758.

[29] J. P. Perdew, J. A. Chevary, S. H. Vosko, K. A. Jackson, M. R. Pederson, D. J. Singh, C. Fiolhais, *Phys. Rev. B* **1992**, 46, 6671.
[30] J. Heyd, G. E. Scuseria, M. Ernzerhof, *J. Chem. Phys.* **2003**, 118, 8207.
[31] M. Imai, M. Kumar, Y. Matsushita, N. Umezawa, *Acta Mater.* **2018**, 148, 492.
[32] M. Kumar, H. Zhao, C. Persson, *Thin Solid Films*, **2013**, 535, 318.
[33] A. Chirila, P. Reinhard, F. Pianezzi, P. Bloesch, A. R. Uhl, C. Fella, L. Kranz, D. Keller, C. Gretener, H. Hagendorfer, R. Erni, S. Nishiwaki, S. Buecheler, A. N. Tiwari, *Nat. Mater.* **2013** 12, 1107.
[34] C. Andres, S. G. Haass, Y. E. Romanyuk, A. N. Tiwari, *Thin Solid Films* **2017**, 633, 141.
[35] C. H. Hsu, D. H. Chen, *Int. J. Hydrog. Energy* **2011**, 36 (24), 15538.
[36] M. Vishwakarma, K. Agrawal, J. Hadermann, B. R. Mehta, *Appl. Surf. Sci.* **2020**, 507, 145043.
[37] S. Zamulko, R. Chen, C. Persson, *Physica Status Solidi (b)* **2017**, 254 (6), 1700084.
[38] C. Persson, *J. Appl. Phys.* **2010**, 107, 053710.
[39] R. Moreno, E. A. Ramirez, G. G. Guzmán, *J. Phys. Conf. Ser.* **2016**, 687, 012041.
[40] M. Dimitrievska, F. Boero, A. P. Litvinchuk, S. Delsante, G. Borzone, A. P. Rodriguez, V. I. Roca, *Inorg. Chem.* **2017**, 56, 6, 3467.
[41] M. Guc, S. Levcenko, V. I. Roca, X. Fontane, M. Y. Valakh, E. Arushanov, A. P. Rodríguez, *J. Appl. Phys.* **2013**, 114, 173507.
[42] J. Tauc, in: J. Tauc (Ed.), *Amorphous and Liquid Semiconductors*, Plenum Press, London and New York, **1974**.
[43] J. Just, M. S. Fella, D. L. Hecht, R. Frahm, S. Schorra and T. Unold, *Phys. Chem. Chem. Phys.* **2016**, 18, 15988.
[44] D. Briggs, *XPS: basic principles, spectral features and qualitative analysis, in: D. Briggs, J.T. Grant (Eds.), Surface analysis by auger and x-ray photoelectron spectroscopy*, IM Publications, Chichester, **2003**.
[45] O. Stroyuk, A. Raevskaya, O. Selyshchev, V. Dzhagan, N. Gaponik, D. R. T. Zahn and A. Eychmuller, *Sci. Rep.* **2018**, 8, 13677.
[46] M. Aono, K. Yoshitake, H. Miyazaki, *Phys. Status Solidi C* **2013**, 10, 7–8, 1058.
[47] J. Brillet, J. H. Yum, M. Cornuz, T. Hisatomi, R. Solarska, J. Augustynski, M. Graetzel, K. Sivula, *Nat. Photonics* **2012**, 6, 824.
[48] L. Wei, Z. Guo, X. Jia, *Catal. Letters* **2021**, 151, 56.
[49] S. B. A. Hamid, S. J. The, C. W. Lai, *Catalysts* **2017**, 7, 93.
[50] M. G. Mali, H. Yoon, B. N. Joshi, H. Park, S. S. Al-Deyab, D. C. Lim, S. Ahn, C. Nervi, S. S. Yoon, *ACS Appl. Mater. Interfaces* **2015**, 7, 21619.
[51] K. Zhang, M. Ma, P. Li, D. H. Wang, J. H. Park, Adv. Energy Mater. 2016, 6 (15) 1600602.
[52] J. Joe, H. Yang, C. Bae, H. Shin, Catalysts 2019, 9, 149.
[53] M. Moriya, T. Minegishi, H. Kumagai, M. Katayama, J. Kubota, K. Domen, *J. Am. Chem. Soc.* **2013**, 135, 3733.
[54] Y. Yang, D. Xu, Q. Wu, P. Diao, *Sci. Rep.* **2016**, 6, 35158.
[55] Z. Chen, H. N. Dinh, E. Miller, *Photoelectrochemical Water Splitting,* Springer, New York, NY **2013**, Ch. 6. (*Pages 70-73*)
[56] M. Vishwakarma, D. Varandani, C. Andres, Y. E. Romanyuk, S. G. Haass, A. N. Tiwari, B. R. Mehta, *Sol. Energy Mater. Sol. Cells* **2018**, 183, 34 (2018).
[57] C. Jiang, S. J. A. Moniz, A. Wang, T. Zhang and J. Tang, *Chem. Soc. Rev.* **2017**, 46, 4645.